Monthly Notices
of the
ROYAL ASTRONOMICAL SOCIETY

MNRAS **456,** 2622–2635 (2016) doi:10.1093/mnras/stv2795

Optical observations of the luminous Type IIn Supernova 2010jl for over 900 d

J. E. Jencson,[1★†] J. L. Prieto,[2,3] C. S. Kochanek,[4,5] B. J. Shappee,[6‡§] K. Z. Stanek[4,5] and R. W. Pogge[4,5]

[1]*Cahill Center for Astronomy and Astrophysics, California Institute of Technology, Pasadena, CA 91125, USA*
[2]*Núcleo de Astronomía de la Facultad de Ingeniería, Universidad Diego Portales, Av. Ejército 441, Santiago, Chile*
[3]*Millennium Institute of Astrophysics, Santiago, Chile*
[4]*Department of Astronomy, The Ohio State University, 140 West 18th Avenue, Columbus, OH 43210, USA*
[5]*Center for Cosmology and AstroParticle Physics (CCAPP), The Ohio State University, 191 West Woodruff Avenue, Columbus, OH 43210, USA*
[6]*Carnegie Observatories, 813 Santa Barbara Street, Pasadena, CA 91101, USA*

Accepted 2015 November 26. Received 2015 November 25; in original form 2015 May 5

ABSTRACT

The luminous Type IIn Supernova (SN) 2010jl shows strong evidence for the interaction of the SN ejecta with dense circumstellar material (CSM). We present observations of SN 2010jl for $t \sim 900$ d after its earliest detection, including a sequence of optical spectra ranging from $t = 55$ to 909 d. We also supplement our late time spectra and the photometric measurements in the literature with an additional epoch of new, late time *BVRI* photometry. Combining available photometric and spectroscopic data, we derive a semi-bolometric optical light curve and calculate a total radiated energy in the optical for SN 2010jl of $\sim 3.5 \times 10^{50}$ erg, confirming the result of Fransson et al. We also examine the evolution of the Hα emission line profile in detail and find evidence for asymmetry in the profile for $t \gtrsim 775$ d that is not easily explained by any of the proposed scenarios for this fascinating event. Finally, we discuss the interpretations from the literature of the optical and near-infrared light curves, and propose that the most likely explanation of their evolution is the formation of new dust in the dense, pre-existing CSM wind after ∼300 d.

Key words: supernovae: general – supernovae: individual: SN 2010jl.

1 INTRODUCTION

Type IIn supernovae (SNe IIn) are a rare class of events, making up only 6–9 per cent of core collapse SNe (e.g. Smartt et al. 2009; Li et al. 2011; Smith et al. 2011a). They are characterized by the presence of strong, composite-profile emission lines of H and He. Generally, the emission line profiles of SNe IIn may consist of narrow-width (NW; ~ 100 km s^{-1}) and intermediate-width (IW; ~ 1000 km s^{-1}) components (Schlegel 1990; Filippenko 1997). The NW component is often explained as arising in dense, slowly expanding circumstellar material (CSM) photoionized by the initial flash of the supernova (SN) explosion (e.g. Chevalier & Fransson 1994; Salamanca et al. 1998; Chugai et al. 2002; Salamanca, Terlevich & Tenorio-Tagle 2002). IW lines arise at early times as either Thomson scatter broadening of the NW lines or emission from cool, accelerated, post-shock CSM gas (e.g. Chugai & Danziger 1994; Chugai 2001; Chugai et al. 2004; Dessart et al. 2009; Smith et al. 2010). The shock interaction of the ejecta with the dense CSM also provides a possible explanation for the extreme optical luminosity of many SNe IIn (Chugai & Danziger 1994).

SN 2010jl was discovered in the galaxy UGC 5189A on 2010 November 3.52 (UT) by Newton & Puckett (2010). It was classified as an SN IIn due to the presence of NW emission lines in a spectrum taken on 2010 November 5 (Benetti et al. 2010; Yamanaka et al. 2010). Smith et al. (2011b) identified a possible luminous blue progenitor star in archival *Hubble Space Telescope* (*HST*) WFPC2 data, but it is not possible to distinguish between a single massive star and a star cluster from these observations. Observations of this region after the SN light fades could be used to differentiate between these possibilities. Regardless, each of the progenitor scenarios explored by Smith et al. (2011b) point to a progenitor with a mass of at least 30 $M_\odot$. Spectropolarimetry results from SN 2010jl two weeks after its discovery indicate possible asymmetry in the explosion geometry, or, more likely, in the CSM (Patat et al. 2011).

Pre-discovery images from the All-Sky Automated Survey (ASAS) North telescope in Hawaii (Pojmański 2002; Pigulski et al.

★E-mail: jj@astro.caltech.edu
† NSF Graduate Fellow.
‡ Hubble Fellow.
§ Carnegie–Princeton Fellow.

2009) also show that SN 2010jl is intrinsically luminous, reaching a peak absolute *I*-band magnitude of ~ -20.5 (Stoll et al. 2011), placing it near the class of ≤ -21 mag 'superluminous SNe' defined by Gal-Yam (2012). Additionally, Stoll et al. (2011) show that the host of SN 2010jl is low metallicity, supporting an emerging trend that optically luminous SNe tend to go off in low-metallicity, low-luminosity hosts (e.g. Kozłowski et al. 2010; Li et al. 2011; Neill et al. 2011). The ASAS images indicate that the explosion likely occurred in early 2010 October. We will refer to days t since the earliest detection of SN 2010jl on 2010 October 9 by ASAS (JD = 245 5479.14; Stoll et al. 2011) throughout this paper.

Andrews et al. (2011) construct a spectral energy distribution (SED) using optical, and near- and mid-infrared photometry of SN 2010jl at $t \sim 90$ d, and find evidence for a $T \sim 750$ K infrared (IR) excess. They interpret the IR excess as evidence for pre-existing dust in the unshocked CSM, heated by radiation from the SN. Similar conclusions were drawn by Fox et al. (2013) based on mid-IR 3.6 and 4.5 μm *Spitzer*/IRAC observations at $t = 253$ d. They derive a temperature of the pre-existing dust of ∼735 K, and a mass of the dust shell of 8.47×10^{-3} M$_\odot$.

Smith et al. (2012) observe a systematic blueshift for the first seven months in the IW component of Hα that arises in the post-shock CSM, indicating the formation of new dust in the post-shock cooling zone of the SN. Their spectra also indicate that the blueshift is stronger at shorter wavelengths, which one would expect if it is the result of dust formation; however, this explanation conflicts with the low dust emission temperature observed by Andrews et al. (2011). An alternative explanation is that the high optical depth continuum continues to block light from the receding side of the post-shock shell, resulting in line profiles that appear blueshifted (Smith et al. 2012).

An extensive data set consisting of *UBVRI* light curves and a sequence of optical spectra for over 500 d was presented in Zhang et al. (2012). Both the slow decline of the light curves and the remarkable strength of the Hα emission with respect to the continuum for over 500 d provide strong evidence for successive interactions of the SN ejecta with a dense, hydrogen-rich CSM. They also observe a systematic blueshift of the line profiles of Hα, but disfavour the interpretation of new dust formation due to a decrease in the blueshift of the line profiles for $t \gtrsim 500$ d, and the lack of a corresponding decline in the optical light curves one would expect from extinction by new dust.

Maeda et al. (2013) claim to find strong evidence for dust formation in SN 2010jl at $t \sim 550$ d. They present near-IR (NIR) spectroscopy and *JHK* photometry, in addition to optical spectroscopy and *BVRI* photometry at similar epochs. They detect a NIR thermal component with temperatures of $T \sim$ 1000–2000 K which was not present at earlier epochs. They also report an increase in the blueshift of Hα to $\gtrsim 700$ km s^{-1} for $t \gtrsim 400$ d, and that the degree of the blueshift is smaller for lines at longer wavelengths. Finally, they point out that the decline in optical luminosity accelerates after ∼1 yr. They conclude that the cumulative evidence provides a strong case for new dust formation in a dense cooling shell formed by the interaction of the SN ejecta and the CSM.

A more complete data set including *uBVRiJHK* photometry, ultraviolet (UV) spectra from *HST*, extensive optical spectroscopy, and spectra in the NIR was presented in Fransson et al. (2014), in which the authors debate the conclusions drawn by Maeda et al. (2013). They derive a 'pseudo-bolometric' (optical through NIR) light curve of SN 2010jl, and show that the NIR component, which they interpret as an echo from pre-existing CSM dust heated by the SN, becomes an increasingly important contribution to the bolometric luminosity with time. They present a sequence of Hα profiles from $t = 31$ to $t = 1128$ d, and claim that the broad component shows smooth, peaked, and symmetric profiles characteristic of electron scattering. The blueshift present in the lines for $t \gtrsim 50$ d is interpreted as a macroscopic bulk velocity due to radiative acceleration of the pre-shock scattering medium by the energetic radiation field of the SN. This interpretation requires no wavelength dependence of the blueshift and is thus inconsistent with the observed wavelength dependence seen by Smith et al. (2012), Maeda et al. (2013), and Gall et al. (2014). From the narrow CSM lines present in their spectra, some of which show a P Cygni absorption component, they infer a CSM velocity of ~ 100 km s^{-1} consistent with a Luminous Blue Variable (LBV) star as a possible progenitor. They find the mass-loss rate to account for the bolometric light curve with CSM interaction to be $\gtrsim 0.1$ M$_\odot$ yr^{-1}, and a total mass loss of $\gtrsim 3$ M$_\odot$.

Borish et al. (2015) present a sequence of $1 - 2.4$ μm NIR spectra from $t = 36$ to 565 d. They observe a progressive blueshift to ~ 700 km s^{-1} of the broad hydrogen lines with time, similar to the evolution seen in the optical hydrogen lines. They also observe a broad, asymmetric component in the He I λλ10830, 20587 lines, and a blue shoulder feature at ~ 5000 km s^{-1}, possibly associated with a high-velocity, He-rich ejecta flow. Similar to the results of Fransson et al. (2014), they observe a $T \sim 1900$ K blackbody feature in the continuum emission at $t = 403$ d, likely associated with dust emission.

Gall et al. (2014) observed SN 2010jl with the VLT/X-shooter spectrograph in a sequence of optical-NIR spectra covering the range 0.3–2.5 μm for $t \lesssim 250$ d, and again on $t = 876$ d. They find evidence for wavelength-dependent extinction in their analysis of the IW emission lines, and interpret this as extinction by newly formed dust. They derive dust extinction curves for SN 2010jl and find evidence for large dust grains in excess of 1 μm in size. They claim that the dust production site transitions from the CSM to the ejecta for $t \gtrsim 500$ d based on the accelerated growth in dust mass at this time.

SN 2010jl was detected by the *Swift* on-board X-ray Telescope (XRT; Burrows et al. 2005) on 2010 November 5.0–5.8 with an inferred X-ray luminosity of $(3.6 \pm 0.5) \times 10^{40}$ erg s^{-1} (Immler, Milne & Pooley 2010). *Chandra* observations were triggered by Chandra et al. (2012a) to observe SN 2010jl on $t = 59$ and 373 d, which demonstrated a high temperature of $\gtrsim 10$ keV for both epochs, and a high absorption column density of $\sim 10^{24}$ cm^{-2} at the first epoch that decreases by a factor of 3 at the second epoch, likely associated with absorption by the CSM.

Ofek et al. (2014) also present X-ray observations of SN 2010jl from *NuSTAR* and *XMM–Newton*, in addition to multi-epoch *Swift*-XRT observations, and public *Chandra* observations (PIs Pooley, Chandra; Chandra et al. 2012b). They also present the PTF *R* and *g* band, and *Swift*-UVOT light curves. They apply a more general version of the model described by Svirski, Nakar & Sari (2012) for an SN shock interacting with an optically thick CSM, assuming spherical symmetry, and find a CSM mass in excess of 10 M$_\odot$. Furthermore, they measure the temperature of the X-ray emission and infer a shock velocity of ~ 3000 km s^{-1}.

In this paper, we present an analysis of extensive optical observations of SN 2010jl over a period of ∼2.5 yr. Our data set adds significant coverage of the spectroscopic time series for SN 2010jl and we evaluate the current physical models proposed in the literature to explain these observations.

The observations, primarily a sequence of optical spectra but including a supplementary epoch of late time *BVRI* photometry, and data reduction procedures are presented in Section 2. In Section 3,

Table 1. Spectroscopic observations of SN 2010jl.

UT date	Phase (d)	Range (Å)	FWHM resolution (Å)	Instrument
2010 Nov. 6	28	3920–6800	3.4	OSMOS 2.4 m Hiltner
2010 Nov. 12	34	3110–5880	3.1	OSMOS 2.4 m Hiltner
2010 Dec. 3	55	3460–9500	7.8	DIS 3.5 m ARC
2010 Dec. 29	81	3660–9100	6.7	WFCCD 2.5 m du Pont
2011 Mar. 12	154	3460–9400	7.5	DIS 3.5 m ARC
2011 Nov. 17	404	3170–9890	2.4	MODS LBT
2012 Jan. 02	450	3460–9500	7.6	DIS 3.5 m ARC
2012 Jan. 20	468	3460–9700	6.8	DIS 3.5 m ARC
2012 Feb. 22	501	3460–9700	6.7	DIS 3.5 m ARC
2012 Mar. 4	512	3830–7020	1.9	DIS 3.5 m ARC
2012 Nov. 22	775	3920–6800	3.1	OSMOS 2.4 m Hiltner
2013 Jan. 10	824	3660–9100	8.7	WFCCD 2.5 m du Pont
2013 Mar. 18	891	3460–9500	6.4	DIS 3.5 m ARC
2013 Apr. 6	909	3660–9100	5.9	WFCCD 2.5 m du Pont

Note. The phase is the number of days since earliest detection on JD = 245 5479.14. The first two spectra were originally presented in Stoll et al. (2011).

we describe our analysis of these data, including the generation of a semi-bolometric, optical light curve in Section 3.2, and a detailed study of the evolution of emission line profiles, particularly Hα, in Section 3.3. Finally, we discuss our physical interpretation of these results and comment on previous interpretations in Section 4. We summarize our conclusions in Section 5.

2 OBSERVATIONS

In this section, we present extensive optical spectroscopy of SN 2010jl and an additional epoch of late time photometry, and describe data reduction procedures.

2.1 Optical spectroscopy

We obtained a total of 12 optical spectra of SN 2010jl using a number of ground-based instruments: the Dual Imaging Spectrograph (DIS) on the 3.5-m ARC telescope at Apache Point Observatory (APO), the Wide Field Reimaging CCD Camera (WFCCD) on the du Pont Telescope at Las Campanas Observatory (LCO), the Multi-Object Double Spectrograph (MODS; Pogge et al. 2010) on the Large Binocular Telescope (LBT) at Mt. Graham International Observatory (MGIO), and the Ohio State Multi-Object Spectrograph (OSMOS; Stoll et al. 2010; Martini et al. 2011) on the 2.4-m Hiltner Telescope at MDM Observatory. These observations began on $t = 55$ d and continue until $t = 909$ d. These spectroscopic observations are summarized in Table 1. Also listed in Table 1 are the two spectroscopic observations originally presented in Stoll et al. (2011), which are used in the analysis discussed below in Sections 3.3 and 3.3.1.

The Hiltner/OSMOS spectrum, the APO/DIS spectra, and the du Pont/WFCCD spectra were reduced using standard tasks in IRAF.[1] The LBT/MODS spectrum was reduced using routines for MODS dual-channel long-slit grating spectra following the 'MODS Basic

[1] IRAF is distributed by the National Optical Astronomy Observatory, which is operated by the Association of Universities for Research in Astronomy (AURA) under cooperative agreement with the National Science Foundation.

Table 2. Photometry of SN 2010jl from JD = 245 6255.

Filter	m (mag)	σ (mag)	M (mag)	σ (mag)	νL_ν ($L_\odot$)
B	19.31	0.11	−14.22	0.11	4.3×10^7
V	18.94	0.05	−14.57	0.05	4.1×10^7
R	17.13	0.05	−16.36	0.05	1.6×10^8
I	17.87	0.05	−15.60	0.05	4.9×10^7

CCD Reduction with *modsCCDRed*' manual.[2] Cosmic rays were removed from the images for all spectra using LACOSMIC (van Dokkum 2001). Wavelength and flux calibrations were performed with comparison lamps and standard star spectra, respectively. The small wavelength zero-point shift between the comparison lamp wavelengths and the observed wavelengths in the spectra was also corrected. Our reduced spectra are available at the online Weizmann Interactive Supernova data REPository (WISeREP; Yaron & Gal-Yam 2012).[3]

The spectra were Doppler corrected for the redshift of the host galaxy ($z = 0.0107$, NED[4]) and for Galactic reddening using $E(B - V) = 0.024$ from Schlafly & Finkbeiner (2011). Following Smith et al. (2011b), no correction was made for host galaxy extinction. Fransson et al. (2014) made an estimate of the reddening for both the host galaxy and the Milky Way from the damping wings of the Lyα absorption in their spectra, and they adopted a value of $E(B - V) = 0.058$ for the total reddening. Our spectra are shown in Fig. 1 showing the log of the flux plus an arbitrary constant for clarity. We also show the two early time OSMOS spectra from Stoll et al. (2011).

2.2 Optical photometry

In order to better interpret the spectra, we performed flux calibrations (see Section 3.2) using published photometry from Stoll et al. (2011) and Zhang et al. (2012), and obtained an additional epoch of late time *BVRI* imaging of SN 2010jl using OSMOS on the 2.4-m Hiltner Telescope at MDM Observatory on $t = 776$ d. The images were reduced using standard tasks in the IRAF CCDPROC package. Flat-fielding was performed using twilight sky flats for each filter taken from $t = 773$ to $t = 776$ d. The photometry of the SN was obtained using the digital photometry reduction program DAOPHOT II with ALLSTAR[5] (Stetson 1987). Due to issues with over subtracting the source, we tested various annuli in DAOPHOT to estimate the background contribution and to minimize contamination from the host galaxy. Instrumental magnitudes were converted to apparent magnitudes using nearby field stars with SDSS DR7 (Abazajian et al. 2009) *ugriz* photometry, converted to standard *BVRI* magnitudes using Ivezić et al. (2007). Our photometric results are summarized in Table 2, where apparent magnitudes are converted to absolute magnitudes by adopting a distance modulus to the host galaxy of 33.43 mag (NED) and using the Galactic extinction corrections from Schlafly & Finkbeiner (2011). *BVRI* magnitudes are also converted to band luminosities, $\nu L_\nu / L_\odot$, using

[2] *modsCCDRed* manual is available here: http://www.astronomy.ohio-state.edu/ MODS/Manuals/MODSCCDRed.pdf

[3] WISeREP spectra are available at: http://wiserep.weizmann.ac.il/

[4] The NASA/IPAC Extragalactic Database (NED) is operated by the Jet propulsion Laboratory, California Institute of Technology, under contract with the National Aeronautics and Space Administration.

[5] Stetson P. B., 2000, User's Manual for DAOPHOT II.

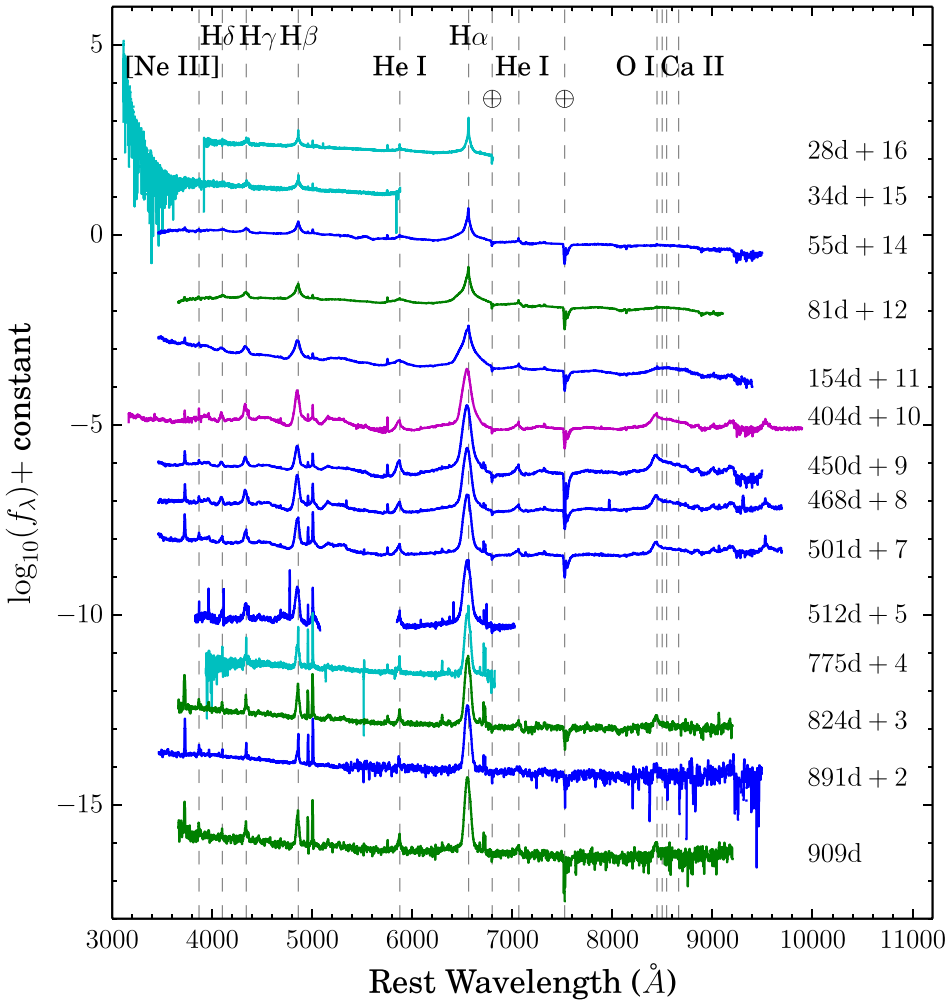

Figure 1. Rest wavelength spectra of SN 2010jl obtained from 2010 November to 2013 April with Hiltner/OSMOS (cyan), APO/DIS (blue), Du Pont/WFCCD (green), and LBT/MODS (magenta). The spectra are corrected for Galactic extinction with $E(B-V) = 0.024$ mag (Schlafly & Finkbeiner 2011). Each spectrum is shifted by the indicated constant for clarity. Days since first detection are also indicated along the right side. Also shown at the top are the two early time OSMOS spectra from Stoll et al. (2011).

the zero-points of the Johnson–Cousins–Glass system from Bessell, Castelli & Plez (1998). Our photometric results are shown in Fig. 2, along with light curves from Stoll et al. (2011), Zhang et al. (2012), Ofek et al. (2014), and Fransson et al. (2014).

3 ANALYSIS

In this section we present the results of our data analysis. In Section 3.1 we examine the new photometric data points presented in this paper in the context of published light curves from the literature. In Section 3.2 we describe the procedure used to derive a semi-bolometric optical light curve for SN 2010jl, and compare its evolution to that of Hα and the NIR luminosity. In Section 3.3 we describe the evolution of the optical spectra, in particular the Hα emission profile (Section 3.3.1).

3.1 *BVRI* light curves and colour evolution

The photometric measurements from 2012 November 23 presented in this paper are added to light curves from the literature as shown in Fig. 2. The light curves also include the pre-discovery *V*- and *I*-band measurements from Stoll et al. (2011), the *BVRI* light curves from Zhang et al. (2012), the PTF *R*-band measurements from Ofek et al. (2014), converted from AB to Vega magnitudes using the conversions by Blanton & Roweis (2007), and the *B*- and *V*-band light curves from Fransson et al. (2014). We note a few discrepancies among the measurements, particularly at late times. Beginning at $t \sim 80$ d, the Fransson et al. (2014) *B* and *V* light curves begin to diverge from the corresponding Zhang et al. (2012) light curves, with the Fransson et al. (2014) measurements $\sim$0.1 mag fainter in *B* and $\sim$0.2 mag fainter in *V*. After the break in the light curve at $t \sim 300$ d, these discrepancies grow to $\sim$1.0 mag, and we note that the Fransson et al. (2014) light curves show a significantly steeper decline in both bands. Our measurements at $t = 776$ d, shown as stars in Fig. 2, are $\sim$0.2 mag fainter in *R* than the PTF measurements and $\sim 0.2 - 0.3$ mag brighter in *B* and *V* than the Fransson et al. (2014) measurements. These discrepancies may be due to difficulties in estimating the background flux as the SN fades and the contribution of the host galaxy becomes more significant.

Fig. 3 shows colour measurements from our *BVRI* photometry as compared to the colour evolution from Zhang et al. (2012) and Fransson et al. (2014). The $B - V$ colour remains mostly constant at $\sim$0.3 mag, consistent with our measurement of $B - V = 0.3 \pm 0.1$ mag at $t = 776$ d. In $B - V$, we again note an $\sim$0.1 mag

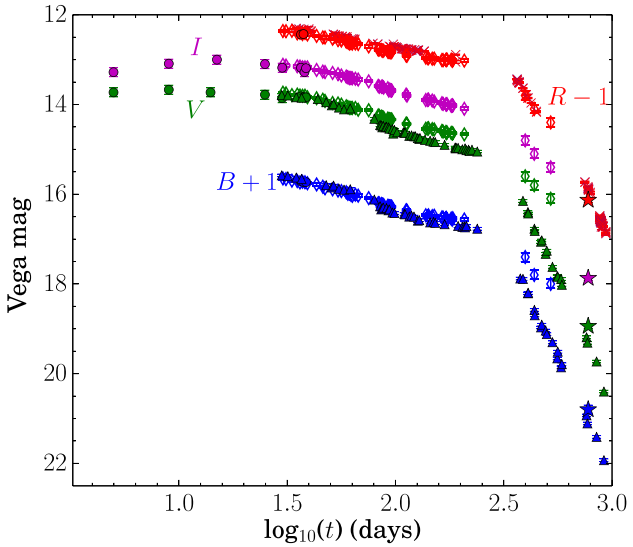

Figure 2. *BVRI* light curves of SN 2010jl. The stars are the new data presented in this paper. Circles are early time measurements from Stoll et al. (2011). The diamonds come from Zhang et al. (2012). *B*- and *V*-band measurements from Fransson et al. (2014) are shown as triangles. The 'X' symbols are the PTF *R*-band measurements from Ofek et al. (2014), converted from AB to Vega magnitudes using the conversions from Blanton & Roweis (2007). Error bars are shown, but can be smaller than the points.

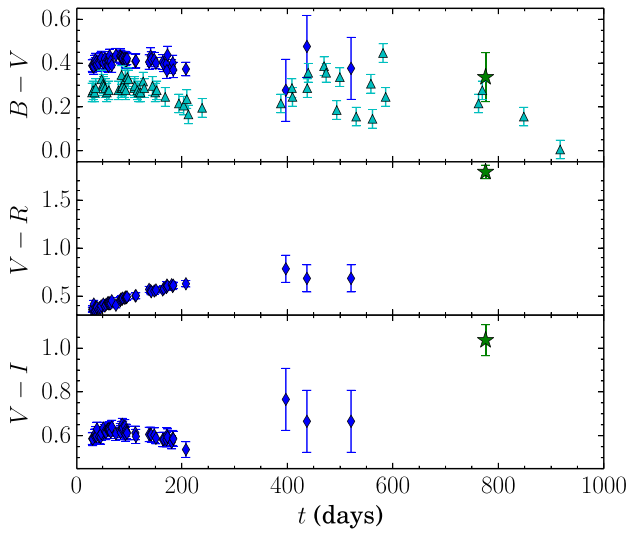

Figure 3. Colour evolution of SN 2010jl. The green stars were obtained using the *BVRI* photometry presented in this paper. The blue diamonds come from Zhang et al. (2012), and the cyan triangles come from Fransson et al. (2014). All measurements were corrected for Galactic reddening using the extinction corrections from Schlafly & Finkbeiner (2011) before computing colours. Error bars are shown, but can be smaller than the points.

discrepancy between the Zhang et al. (2012) and Fransson et al. (2014) measurements. The $B - V$ colour also appears to fall off towards the blue for $t \gtrsim 800$ d in the Fransson et al. (2014) measurements, which may be associated with the bluer continua present in the last few spectra, possibly from host galaxy contamination. In $V - R$, the colour becomes redder with time, increasing from $V - R \sim 0.4$ mag at early times to our measurement of $V - R = 1.8 \pm 0.1$ mag at $t = 776$ d. This is consistent with the continued strength of the Hα line (contained in the *R* band) relative to the continuum at late times (see Sections 3.3 and 3.3.1). We also note that $V - I$ becomes redder, increasing from $V - I \sim 0.6$ mag at early times to our late time measurement of $V - I = 1.0 \pm 0.1$ mag.

Table 3. Optical luminosity.

JD −240 0000	Phase (d)	L (erg s^{-1})	L ($L_\odot$)
55479.14	0.00	1.6(2) × 10^{43}	4.2(4) × 10^9
55484.13	4.99	1.6(1) × 10^{43}	4.1(3) × 10^9
55488.12	8.98	1.7(1) × 10^{43}	4.4(3) × 10^9
55493.14	14.00	1.7(2) × 10^{43}	4.4(4) × 10^9
55494.12	14.98	1.7(2) × 10^{43}	4.4(4) × 10^9
55504.10	24.96	1.6(1) × 10^{43}	4.1(3) × 10^9
55509.10	29.96	1.5(1) × 10^{43}	3.9(4) × 10^9
55509.13	29.99	1.4(1) × 10^{43}	3.7(3) × 10^9
55515.75	36.61	1.56(4) × 10^{43}	4.01(9) × 10^9
55516.75	37.61	1.58(4) × 10^{43}	4.0(1) × 10^9

Note. The phase is the number of days since earliest detection on JD = 245 5479.14. Table 3 is published in its entirety in the electronic edition of this journal. A portion is shown here for guidance regarding its form and content.

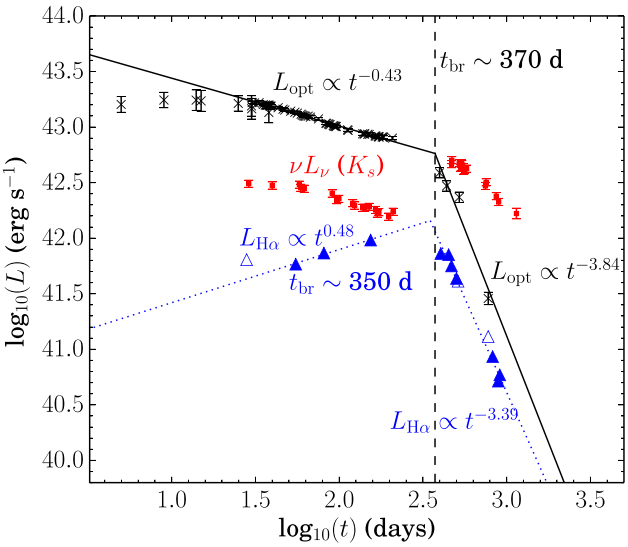

Figure 4. The semi-bolometric optical light ('X' symbols), Hα (triangles), and *K*-band luminosities (squares) of SN 2010jl. The error bars, representing only statistical uncertainties for the derived optical points, are shown but can be smaller than the points. Power-law fits to the optical light curve and Hα are shown as black dashed and blue dotted lines. The Hα luminosities associated with open triangles are approximate and are not included in the fits.

3.2 Semi-bolometric optical light curve

We generated a semi-bolometric, optical light curve (3460–9700 Å) using a combination of the spectra and available photometric data from this paper, Stoll et al. (2011) and Zhang et al. (2012). We also used the 12 optical spectra from Zhang et al. (2012), obtained from WISeREP. The shape of the optical SED was estimated as a function of time by interpolating the observed spectra, and put on an absolute flux scale using synthetic photometry. Using this model of the SED with time, synthetic spectra were produced for days that had available photometry, and integrated to give the optical luminosity for each day. The resulting light curve is tabulated in Table 3 and shown in Fig. 4. Statistical uncertainties were estimated for each point using a bootstrap technique. The entire analysis was run

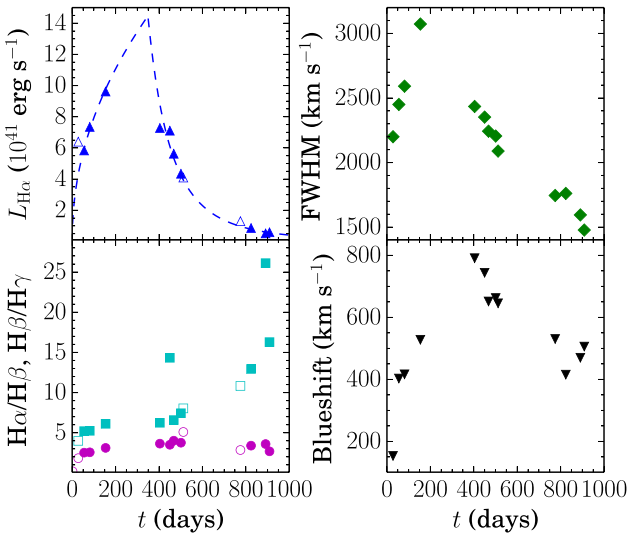

Figure 5. The evolution of various features of the Balmer emission lines. As in Fig. 4, open points are only approximate. Upper left: the integrated Hα luminosity and corresponding power-law fits. Lower left: the Hα/Hβ and Hβ/Hγ luminosity ratios are shown as cyan squares and magenta dots, respectively. Upper right: the FWHM of the IW component of Hα. Lower right: the blueshift of the IW component of Hα measured as the median velocity of the IW profile.

10 000 times, allowing the input photometry to vary with Gaussian distributed noise defined by the reported uncertainties. Trapezoidal integration of this light curve in time from $t = 0$ to 776 d gives an estimated total radiated energy in the optical of $(3.50 \pm 0.03) \times 10^{50}$ erg. We caution that the uncertainty reported here is only an estimate of the statistical uncertainty from the bootstrap procedure, and does not include systematic error such as host galaxy contamination and the gap in the data when the SN was too close to the Sun to be observed between $t \sim 200$ and 400 d. This confirms the result of Fransson et al. (2014) of $\sim 3.3 \times 10^{50}$ erg in the 3600–9000 Å range from $t = 0$ to 920 d. In addition to the difference in wavelength and time coverage, we point out again the discrepancies between the Zhang et al. (2012) photometry used in this analysis and the photometric measurements used by Fransson et al. (2014) (see Section 3.1), which may be responsible for the small difference in the derived optical energy output.

Overplotted as black dashed lines in Fig. 4 are power-law fits to the derived optical light curve. The points from $t \sim 20$ to $\sim$370 d were best fitted with a power-law decay, given by $L_{\rm opt}(t) = 1.02 \times 10^{43}(t/100\,{\rm d})^{-0.43}$ erg s^{-1}, where $L_{\rm opt}$ is the optical luminosity and t is the time since the earliest detection of this event. The remaining late time points through $t = 776$ d were fitted with an $L_{\rm opt}(t) = 6.01 \times 10^{42}(t/370\,{\rm d})^{-3.84}$ erg s^{-1} power law. The break in the light curve, defined as the intersection of the two power-law fits, occurs at $t_{\rm br} \sim 370$ d after first detection. The lack of data near this epoch makes it difficult to accurately constrain the timing of the break. Possible interpretations of the decline in the optical light curve at late times are discussed in Section 4.3.

For comparison in Fig. 4, we also show the Hα luminosity as a function of time (also see Fig. 5 and Section 3.3 for further discussion) and the corresponding power-law fits. Luminosities corresponding to open triangles are only approximate due to insufficient wavelength coverage in the spectra for proper flux calibration with synthetic photometry and are not included in the power-law fits described below. In contrast to the integrated optical luminosity, the early time Hα luminosity follows an increasing power law given by $L_{\rm H\alpha}(t) = 7.94 \times 10^{41}(t/100\,{\rm d})^{0.48}$ erg s^{-1} until at least $t = 154$ d. At late times, the Hα light curve is well fitted by steep power-law decay given by $L_{\rm H\alpha}(t) = 1.43 \times 10^{42}(t/350\,{\rm d})^{-3.39}$ erg s^{-1}. The slope of the Hα light curve remains slightly shallower than that of the optical light curve at late times. The break in the Hα light curve, defined by the break in the power-law fits, occurs at $t \sim 350$ d, near the time of the break in the full optical light curve.

Finally, we also show the K-band data from Fransson et al. (2014) in Fig. 4, converted from 2MASS system magnitudes to νL_ν band luminosities using a K_s flux zero-point of $F_{\nu,0} = 666.8$ Jy at $\nu = 1.390 \times 10^{14}$ Hz (Cohen, Wheaton & Megeath 2003). As noted by Fransson et al. (2014), the NIR luminosity becomes dominant over the optical after the break in the light curve at $\sim$370 d.

3.3 Spectral evolution of SN 2010jl

Similar to the results of previous studies, the major features of the spectra of SN 2010jl shown in Fig. 1 remain mostly unchanged throughout its evolution, with some notable exceptions. The continuum of each spectrum can be approximated by a $T \sim$6000–8000 K blackbody spectrum; however, we note a slight bluing of the continuum at late times which may be due to contaminating light from the host galaxy as the SN fades. We also detect [O III] narrow emission features near 5000 Å, which become more prominent at late times and are also likely due to contamination from the underlying star-forming region. Host galaxy spectra of two H II regions $\sim$7 arcsec north and south of the position of the SN from Stoll et al. (2011) clearly show strong, narrow Balmer and [O III] emission features indicative of recent star formation. A number of spectroscopic parameters, discussed below are given in Table 4.

The most prominent lines in the spectra are the strong, broad Balmer emission features. We detect the Hα through Hδ lines individually, while lines bluer than Hδ are blended together. Superimposed on the broad Balmer lines, we detect narrow blueshifted P Cygni absorption in the MODS spectrum on $t = 404$ d and in the DIS spectrum on $t = 512$ d, but these components are not resolved in the rest of our lower resolution spectra. The width of the P Cygni component measured from the peak to the minimum is typically $\sim$100 km s^{-1}. The evolution of the Hα profile is discussed in detail in Section 3.3.1. The broad He I $\lambda\lambda$5876, 7065 lines also show evidence for a superimposed narrow component.

As noted previously in a number of studies (e.g. Smith et al. 2012; Zhang et al. 2012; Fransson et al. 2014; Gall et al. 2014), the Balmer lines, particularly Hα, show a remarkable growth in strength relative to the continuum for $t \lesssim 400$ d as indicated by the equivalent width (EW) of the lines, measured using the IRAF task SPLOT. From $t = 28$ to 450 d, the magnitude of the EW of Hα strengthened from 167 ± 5 Å to 3400 ± 500 Å, and it remained strong at $\sim$2000 Å in each of the later spectra (see Table 4). Similarly, the magnitude of the EW of Hβ strengthened from 35 ± 2 Å to 300 ± 40 Å in approximately the first 400 d. The increase in strength of the Balmer lines is indicative of interactions of the SN ejecta with a dense hydrogen-rich CSM. We also note that the He I lines show similar evolution to that of the Balmer lines, but are weaker in strength.

As given in Table 4 and shown in the left column of Fig. 5, we calculate the Hα luminosity, as well as the Hα/Hβ and Hβ/Hγ luminosity ratios. Luminosities were calculated by subtracting a linear approximation to the continuum under the line, and then integrating the flux for the full width of the line. For $t = 28$, 34, 512, and 775 d, the luminosity measurements are only approximate due to insufficient wavelength coverage in the spectra for absolute

Table 4. Spectroscopic parameters of SN 2010jl.

Phase	EW (Å) Hα	EW (Å) Hβ	EW (Å) He I (5876 Å)	EW (Å) He I (7065 Å)	Hα luminosity (10^{41} erg s^{-1})	Hα/Hβ	Hβ/Hγ
28	−167 (5)	−35 (2)	−14 (4)	···	6.4	4.0	1.8
34	···	−40 (3)	···	···	···	···	1.6
55	−310 (10)	−59 (6)	−24 (1)	−11 (1)	5.8	5.2	2.5
81	−480 (20)	−80 (6)	−41.6 (0.7)	−18 (3)	7.3	5.2	2.6
154	−950 (40)	−134 (9)	−54.6 (0.8)	−22 (2)	9.6	6.1	3.1
404	−2700 (100)	−300 (40)	−51 (2)	−24 (1)	7.3	6.2	3.6
450	−3400 (500)	−150 (20)	−75 (2)	−36 (2)	7.1	14.3	3.5
468	−2400 (300)	−270 (30)	−42 (1)	−20 (1)	5.6	6.6	4.0
501	−2000 (200)	−190 (30)	−33.7 (0.9)	−19 (2)	4.3	7.4	3.8
512	−2400 (300)	−200 (10)	···	···	4.1	8.0	5.1
775	−1900 (200)	−98 (5)	−18 (2)	···	1.3	10.8	2.9
824	−2400 (200)	−126 (5)	−24 (2)	−18 (3)	0.86	12.9	3.4
891	−2100 (100)	−52 (2)	−11 (2)	−12 (2)	0.52	26.1	3.6
909	−3000 (200)	−150 (7)	−34 (2)	−14 (4)	0.59	16.3	2.7

Note. The phase is the number of days since earliest detection on JD = 245 5479.14. 1-σ uncertainties are given in parentheses. The luminosities at t = 28, 34, 512 and 775 d are only approximate due to insufficient spectral coverage for flux calibration with synthetic photometry.

flux calibration using available photometry. We find similar results to Fransson et al. (2014) (compare with their fig. 12). The Hα luminosity increases by a factor of ∼1.5 from $t = 28$ to 154 d. After the break in the light curve, which occurred when the SN was close to the Sun, the luminosity drops again, and continues to fall by a factor of ∼10 between $t \sim 400$ and $t \sim 900$ d. From the power-law fits shown in the figure and discussed above in Section 3.2, the maximum in the Hα luminosity likely occurs at $t \sim 350$ d. This is ∼10 d earlier than the date found by Fransson et al. (2014), but the lack of data between $t \sim 200$ and $t \sim 400$ d makes it difficult to put strong constraints on this date.

As shown in Fig. 5, the Hα/Hβ ratio increases from ∼5 to ∼15 between $t = 28$ to 909 d. The Hβ/Hγ ratio is largely constant, but increases slightly from ∼1.8 to ∼4 between $t = 28$ and 512 d, and then decreases slightly again to ∼3.0 from $t \sim 800$ to ∼900 d. We note that the Hα/Hβ = 14.3 point at $t = 450$ d appears somewhat high compared to the other points around this epoch. The increase in the Balmer decrement at this epoch is, in fact, visible in the $t = 450$ d spectrum in Fig. 1, as there appears to be less flux in the Hβ line compared to the neighbouring epochs. Measurements of the Balmer decrement may be affected by a number of uncertain factors, including accurate extraction and flux calibration of the spectra, and contamination from the Balmer emission of the underlying star-forming region. Interpretations of this apparently high value of Hα/Hβ lie outside the scope of this paper, so we do not attempt to verify this measurement further.

An obvious change in the appearance of the spectra is the development of blended Ca II IR triplet emission (λλ8498, 8452, 8662). These lines are absent in the earliest spectra, and begin to develop by $t = 81$ d. The Ca II IR triplet is a more prominent feature in the spectra by $t = 154$ d. These emission features may be blended with a number of other lines including the O I λ8446 feature. We also detect the presence of [Ne III] λ3865.9 in each of our spectra with sufficient wavelength coverage.

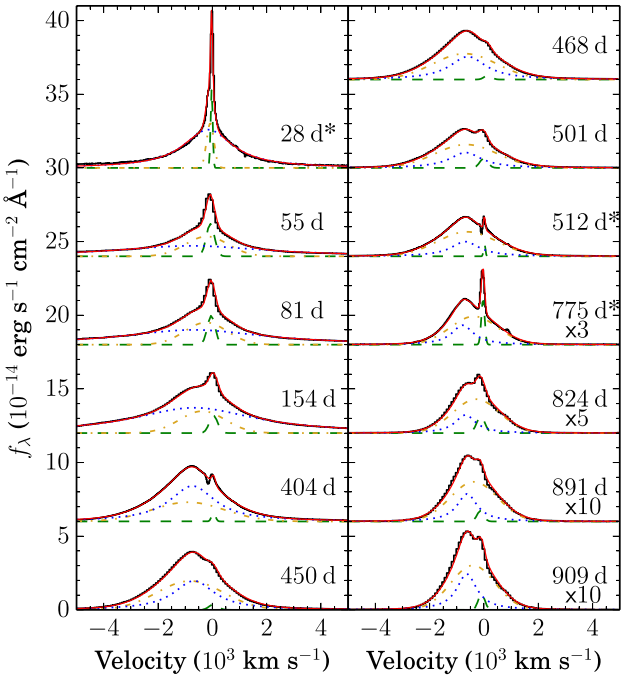

Figure 6. The continuum-subtracted Hα profiles are shown as black histograms, where 0 km s^{-1} corresponds to the host galaxy rest frame wavelength of Hα. The components of each fit (a NW Gaussian, an IW Gaussian, and an IW Lorentzian) are shown as green dashed, yellow dot–dashed, and blue dotted lines, respectively. The best fit to the data is shown as the red curve. Each profile is shifted up by 6×10^{-14} erg s^{-1} cm^{-2} Å^{-1} from the one below, and the last four profiles have also been multiplied by the factor shown in the lower right corner along with phase for clarity. For the days indicated with asterisks, the fluxes are only approximate, corresponding to the open points in Fig. 4.

3.3.1 *Evolution of the Hα emission profile*

The evolution of the Hα emission line is illustrated in Fig. 6 from $t = 28$ to $t = 909$ d. A summary of the spectroscopic parameters of the emission features, including Hα, is given in Table 4. As discussed in Section 3.3, a remarkable feature of the Hα emission is the increase in the EW of this line until $t = 450$ d, and the continued strength of the line with respect to the continuum throughout the rest of the spectra, indicating strong, successive interactions of the SN ejecta with a dense hydrogen-rich CSM.

Table 5. Hα profile component parameters.

Phase	Hα component FWHM (km s^{-1}) NW Gauss	IW Gauss	IW Lorentz	IW Full	Shift (km s^{-1})
28	90	320	2200	2200	−153
55	360	1850	6660	2450	−403
81	340	1850	6340	2590	−417
154	360	1990	5470	3070	−528
404	170	3140	2030	2430	−791
450	390	2860	1810	2350	−744
468	320	2770	1620	2240	−651
501	350	2590	1430	2210	−663
512	80	2060	1260	2100	−646
775	150	2020	970	1750	−531
824	360	2020	910	1760	−416
891	290	2040	890	1590	−470
909	280	1910	890	1480	−506

Note. The phase is the number of days since earliest detection on JD = 245 5479.14. The shift is measured as the median of the full IW component.

To examine the evolution of the Hα profile in detail, we performed multi-component fits to the profiles at each epoch using a Levenberg–Marquardt least-squares minimization algorithm. A linear approximation to the continuum near the line was subtracted from each profile before performing the fits. We find the profiles to be best fitted by three separate components: an NW Gaussian, an IW Gaussian, and a broad or IW Lorentzian. The results of our fits are superimposed on the data in Fig. 6, and the parameters for each component, including the full IW component (sum of the IW Gaussian and IW Lorentzian), are given in Table 5. Previous work decomposed the Hα profile into a two-component profile consisting of an NW component with full width at half-maximum (FWHM) of $\lesssim$1000 km s^{-1} and an IW component with FWHM velocity ∼2000–3500 km s^{-1} (e.g. Patat et al. 2011; Smith et al. 2011b, 2012; Zhang et al. 2012; Fransson et al. 2014). In this data set we find evidence for an NW and IW component, but we are unable to achieve satisfactory fits of the peaks and wings of the profiles simultaneously using only two components. Instead, we find that the IW component is itself usually best fitted by two separate components, an IW Gaussian and an IW Lorentzian. The need for the extra component is illustrated further by the emerging asymmetry of the IW component at late times (see Fig. 8 and discussion below).

The centre of the NW Gaussian component for each Hα profile is typically consistent with 0 ± 100 km s^{-1} relative to the rest frame of the host galaxy. In our highest resolution spectra, the LBT/MODS spectrum from $t = 404$ d and the APO/DIS spectrum from $t = 512$ d, we see that the NW component is actually a P Cygni component consisting of both emission and blueshifted absorption with a typical width of ∼100 km s^{-1} measured from peak to minimum. For these profiles, the NW Gaussian is unable to fit the absorption component and is only representative of the emission component of the narrow P Cygni profile. In the lower resolution spectra, the P Cygni profile is unresolved, and is fit by the NW Gaussian with a typical FWHM of ∼300 km s^{-1}. At late times as the SN fades, the NW component may suffer from significant contamination from the underlying star-forming region.

In the earliest profile from $t = 28$ d, the NW component of the line is best fitted by both Gaussian components, one with FWHM velocity of ∼90 km s^{-1} and one with FWHM velocity of ∼320 km s^{-1}. This may be due to a partially resolved, narrow P Cygni component, resulting in the observed bump on the blue side of the narrow peak. The IW component of the profile from $t = 28$ d can be approximated by a single IW Lorentzian with FWHM velocity of ∼2200 km s^{-1}.

In the subsequent profiles, the IW component, composed of the IW Gaussian and IW Lorentzian, shows a number of important changes as the profile evolves. In the profiles from $t = 55$, 81, and 154 d, the high-velocity wings of the IW component are dominated by a broader (FWHM ∼6000 km s^{-1}) Lorentzian component. By $t = 404$ d the high-velocity wings have vanished, and the IW Lorentzian component becomes considerably narrower (FWHM $\lesssim$2000 km s^{-1}). By $t = 450$ d, the full IW component begins to be more dominated by the Gaussian component (FWHM ∼2000–3000 km s^{-1}). The FWHM of the IW component is plotted in the upper right panel of Fig. 5 as a function of time. The IW component increases in FWHM to ∼3070 km s^{-1} at $t = 154$ d, before beginning to decrease for $t \geq 404$ d towards ∼1500 km s^{-1} at $t = 909$ d. We note the qualitative similarities in the evolution of the Hα IW component FWHM and the integrated Hα luminosity shown in the upper left panel of Fig. 5.

The profile is mostly symmetric in the Hiltner/OSMOS spectrum on $t = 28$ d. By $t \sim 50$ d, however, the profiles show a progressive enhancement towards the blue, while the red side appears suppressed. Confirming the results of Smith et al. (2012), Zhang et al. (2012), Maeda et al. (2013), Fransson et al. (2014), and Gall et al. (2014), we note a progressive blueshift in the profiles, measured as the median velocity of the full IW component. The blueshift of the IW component of Hα is shown in the bottom right panel of Fig. 5. The profile becomes significantly blueshifted with an IW component median velocity of ∼400 km s^{-1} on $t = 55$ d, and becomes more blueshifted with a median velocity of ∼800 km s^{-1} on $t = 404$ d. For $t > 404$ d, the IW component becomes less blueshifted again, with a median velocity of ∼500 km s^{-1} in the last profile on $t = 909$ d.

The change in shape of the Hα profile with time is illustrated in the top row of Fig. 7. In the top left panel, the profiles are scaled to match in the velocity range from −1200 km s^{-1} to −1000 km s^{-1}. By $t = 81$ d the profile shows signs of a relative deficit on the red side of the IW component, and this trend continues until $t = 154$ d. The profile from $t = 404$ d is shown in black and no longer exhibits high-velocity wings on either the red or blue side. A similar trend is observed for the Hβ and Hγ emission line profiles, shown in the middle left and lower left panels, respectively. The late time evolution of the IW component Hα, shown in the top right panel of Fig. 7, changes significantly for $t \geq 404$ d. The profiles, now scaled to match near their peaks, continue to narrow with time, and this effect appears more prominent on the blue side of the peak. This results in profiles which appear asymmetric about the peak by $t = 775$ d.

In Fig. 8, we analyse the symmetric properties of the Hα profiles in detail. The continuum-subtracted profiles are shown in black as in Fig. 6, but the NW Gaussian component has now been subtracted for clarity. The reflection of the profile about the peak of the IW component is then shown in orange for comparison so that for a symmetric profile the orange and black curves will line up with each other. Similar to the results of Fransson et al. (2014), the profiles appear largely symmetric before $t = 775$ d. We note some asymmetry from $t = 28$ to 154 d, where the flux to the red side of the peak appears suppressed, but it is possible that this is due to uncertainties in estimating and subtracting the continuum. This asymmetry continues in the day 404, 450, and 468 profiles, but appears less pronounced. The profiles from $t = 775$ d onwards, in contrast, show a clear asymmetry as flux that was once suppressed appears to return to the red side of the profile. This asymmetry, which has not been noted in any previous study, persists in the three

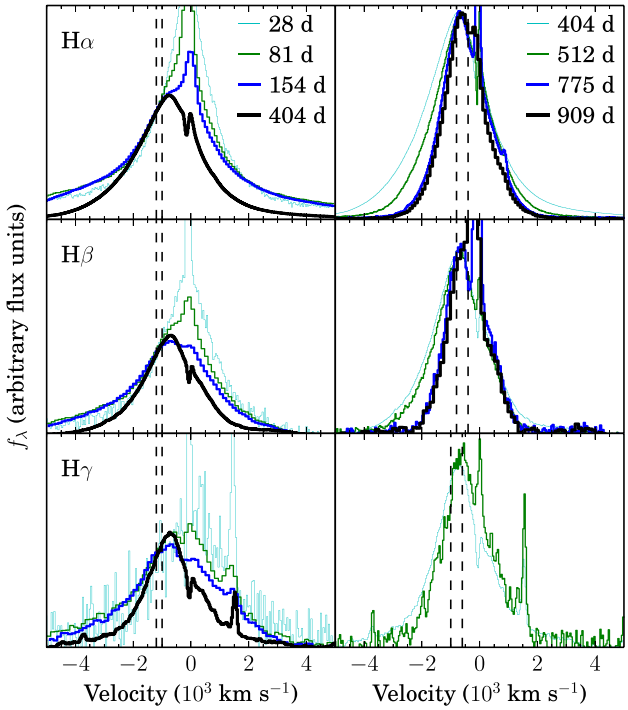

Figure 7. Representative sequence of emission line profiles for Hα (upper), Hβ (middle), and Hγ (lower). Early time profiles are shown in the left column, and late time profiles are shown in the right column. Profiles are scaled to match in the velocity range indicated by the dashed vertical lines in each panel. The Hγ profiles from $t = 775$ and 909 d are not included due to low signal-to-noise ratio.

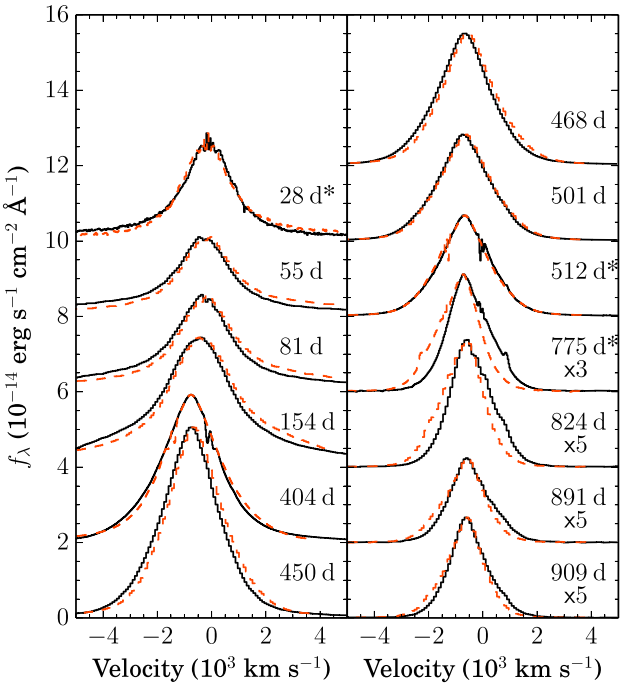

Figure 8. The continuum subtracted Hα profiles after subtracting the NW component for clarity (black). The reflection of each profile about the IW component peak is shown as orange dashed curves. Each profile is shifted up by 2×10^{-14} erg s^{-1} cm^{-2} Å^{-1} from the one below, and the last four profiles have also been multiplied by the indicated factor for clarity. Days since the earliest detection are listed for each profile. For the days indicated with asterisks, fluxes are only approximate as in Fig. 6. Note that the profiles appear approximately symmetric until at least $t = 512$ d, after which they exhibit an enhancement in flux to the red.

remaining profiles, but again becomes noticeably less pronounced with time.

A number of scenarios have been proposed to explain the evolution of the Hα profile, and we examine these possible interpretations below in Section 4.2.

4 DISCUSSION AND PHYSICAL INTERPRETATION

Here we discuss the physical implications of the observed properties of SN 2010jl presented above, and provide additional commentary on physical interpretations previously presented in the literature.

4.1 The NW CSM lines

We observe the presence of narrow spectral emission features in the Balmer series as well as in the optical He I λλ5876, 7065lines. We interpret this as emission from slow-moving gas in the CSM, photoionized by light from the SN. In the higher resolution spectra from $t = 404$ and 512 d, the narrow component of the Balmer lines exhibit blueshifted P Cygni absorption by the expanding foreground CSM gas. The width of the P Cygni component, measured from peak to minimum, is typically ∼100 km s^{-1}, which we take as an estimate of the CSM expansion velocity. This confirms previous estimates of the CSM velocity, and the suggestion of an LBV star as a possible progenitor (Smith et al. 2011b; Fransson et al. 2014).

4.2 The IW lines

As discussed above in Sections 3.3 and 3.3.1, the broad emission lines of H and He show a remarkable growth in strength until $t \sim$ 450 d and clearly indicate strong, successive interactions between the SN ejecta and dense, hydrogen-rich CSM. This further confirms the result of similar observations of SN 2010jl that have been discussed at length in the literature (e.g. Smith et al. 2012; Zhang et al. 2012; Fransson et al. 2014; Gall et al. 2014).

The IW component of the Balmer lines, especially Hα, have been of particular interest because they show some evidence for newly formed dust in the post-shock shell of the SN, but not all lines of evidence are consistent with this interpretation.

In our earliest spectrum from $t = 28$ d, the IW component of Hα is well approximated by a single Lorentzian with a FWHM velocity of ∼2200 km s^{-1} (Fig. 6), which is characteristic of the scattering of Hα photons by thermal electrons in an optically thick CSM. This result is consistent with the early time findings of Smith et al. (2012). Soon after, however, the IW Balmer profiles begin to show significant attenuation of the redshifted flux and a progressive blueshift of the line centre with time until at least $t = 154$ d. Based on similar findings, Smith et al. (2012) proposed that dust formation in the cool, post-shock shell of the SN may be obscuring redshifted photons from interactions on the far side of the SN. Gall et al. (2014) observed similar attenuation of redshifted photons and progressive blueshifts of the line centres in a number of IW lines for approximately the first 240 d. They also show that this blueshift is stronger

at shorter wavelengths, which would be expected if dust formation were responsible. Maeda et al. (2013) advocate for post-shock dust formation as the mechanism responsible for the profile shapes with similar findings at $t \sim 500$ d. This interpretation is dependent on the assumption, though, that early time profiles accurately represent the intrinsic, unattenuated line profiles throughout their evolution, which may not be the case.

As is apparent in Fig. 7, the profile shape and evolutionary trend of the Balmer emission features have changed significantly by $t = 404$ d. The underlying broad component (FWHM velocity $\sim$6000 km s^{-1}) present in earlier spectra has vanished, and the profiles continue to narrow with time throughout the remaining spectra. Rather than progressive attenuation of the red side of the profiles, we now see flux return to the red side of the profile, resulting in profiles which appear very asymmetric about the peak velocity by $t = 775$ d (Fig. 8). The profiles remain blueshifted (i.e. the majority of the line flux still falls to the blue of the host galaxy velocity) even though the degree of the blueshift appears to be decreasing for $t \lesssim 400$ d. These results are apparently inconsistent with the scenario of continued post-shock dust formation at late times, since one would expect a progressive blueshift as light from the receding side of the SN is increasingly blocked by newly formed dust.

Fransson et al. (2014) claim that even as the Hα profiles become more blueshifted, they retain a symmetric shape characteristic of electron scattering. They invoke electron scattering as the origin of the profile shape, with a macroscopic bulk velocity towards the observer in the scattering medium to explain the blueshift of the IW component, and reject dust formation scenarios altogether. This interpretation is inconsistent with the observed wavelength dependence of the blueshift observed by Smith et al. (2012), Maeda et al. (2013), and Gall et al. (2014). Furthermore, although the line profiles appear at least approximately symmetric about the peak velocity for the first $t \sim 500$ d, the clear asymmetry present in the profiles after $t = 775$ d (see Fig. 8) cannot be accounted for by electron scattering alone. The appearance of asymmetric and shifted line profiles could be due to asymmetries in the explosion or CSM geometries. Spectropolarimetry results from Patat et al. (2011) also indicated an asymmetric geometry is likely, but we do not explore this possibility further in this paper.

The formation of emission line profiles is dependent on numerous factors, including multiple velocity components and emission/absorption mechanisms. Additionally, when examining scenarios involving obscuration by newly formed, or pre-existing dust, it is impossible to know the true line profile for each epoch, and assumptions about intrinsic profile shape must be made. For these reasons, although the line profile evolution appears inconsistent with the post-shock dust formation scenario at late times, we find it difficult to rule out any scenario based solely on the shapes and evolution of emission line profiles.

We emphasize the distinction between the post-shock cooling zone dust formation scenarios discussed in the context of emission line profiles and the reformation of dust in the dense CSM wind. In both scenarios, one expects a drop in the optical light curve due to increasing extinction, and the development of a corresponding IR-excess due to radiation from the newly formed dust. Dust which is formed outside of the shock interaction radius, though, will not shift or modify the shape of emission lines, while dust formed inside this radius preferentially blocks redshifted photons from the receding side of the SN. Evidence from the light curves of SN 2010jl regarding the presence of newly reformed or pre-existing dust in the dense CSM wind is discussed in Section 4.3.

4.3 The optical and NIR light curves

As is evident from Fig. 4, the optical light curve of SN 2010jl displays a clear two-stage evolution. After the peak in the optical luminosity at $t \sim 20$ d, the light curve shows a steady decline which is well fitted by an $L_{\rm opt}(t) = 1.02 \times 10^{43} (t/100\,{\rm d})^{-0.43}$ erg s^{-1} power-law decay for at least $t \lesssim 200$ d. At $t \sim 400$ d, the light curve shows a clear break and is now well fitted by a much steeper power-law decay given by $L_{\rm opt}(t) = 6.01 \times 10^{42} (t/370\,{\rm d})^{-3.84}$ erg s^{-1}. Based on the intersection of the power-law fits, the break in the light curve occurs at $t \sim 370$ d. At essentially the same time, the near-IR luminosity rises rapidly so that the evolution of the bolometric luminosity changes little. A problem in the models of SN 2010jl to date is that they do not provide a natural explanation of this transition.

Ofek et al. (2014) lacked information on the near-IR evolution and based their model of the bolometric light curve as a simple correction to the PTF R-band light curve. Thus, the break in the optical light curve was interpreted as a rapid drop in the luminosity being produced by the CSM interactions. They considered three possibilities. First, the shock speed, and hence the luminosity, will drop rapidly once the swept up CSM mass begins to exceed the ejected mass (the so-called 'snow-plow' phase). Secondly, the shock could simply have reached the edge of the dense regions of the CSM. Finally, the CSM density eventually drops to the point where cooling becomes inefficient (the slow cooling stage) and a decreasing fraction of the shock energy is converted to optical photons. They rule out the last solution based on their estimate of the CSM densities, and prefer the first possibility to the second. However, with the addition of the information on the near-IR emission, there is no dramatic drop in the bolometric luminosity to be explained, or one must introduce some independent process to explain the sudden rise in the near-IR emission seen by Andrews et al. (2011), Maeda et al. (2013), Fransson et al. (2014) and Gall et al. (2014).

Fransson et al. (2014) interpret the two evolutionary phenomena as being unrelated. The optical luminosity drops because the shock is reaching the edge of the regions with a dense CSM or, as proposed by Ofek et al. (2014), the shock slows as the swept up CSM mass becomes comparable to the ejecta mass, while the near-IR emission is caused by an echo from pre-existing dust radiatively heated by light from the SN peak. The first problem with this interpretation is that it requires remarkable coincidences in timing and energetics because the near-IR emission has to rise just as the optical emissions drop while maintaining a smooth evolution of the bolometric luminosity. The second problem, as discussed by Fransson et al. (2014), is that the timing requires the inner edge of the dust shell to be at $R_{\rm in} \sim 6 \times 10^{17}$ cm, which makes it very difficult to have dust grains hot enough to produce the near-IR emission. The observed temperatures are $T_{\rm d} \simeq 1500$–2000 K while we estimate that $a = 0.1\,\mu$m grains would have temperatures of only $T_{\rm d} = 950/800$ K for graphite/silicate Laor & Draine (1993) grains. Fransson et al. (2014) argue that this can be solved by making the grains very small, but even for a grain size of $a = 10^{-3}\,\mu$m, we estimate dust temperatures of only $T_{\rm d} = 1100/680$ K for graphitic and silicate grains. Furthermore, for grains created in a wind, or any ejecta, there is a strong correlation between the grain size and the allowed optical depth because both are directly dependent on the density – in essence $\tau \propto a \propto \dot{M}$. In the models of Kochanek (2014), a wind producing such small grains would then have a negligible optical depth at these large radii and so could not support the significant optical depth needed to produce the observed near-IR flux as an echo. Even if we are generous, the original dust-forming

wind would have had at most $\tau_V \simeq 1$ and the optical depth of this large radius shell would be smaller by $R_{form}/R_{in} \simeq 0.01$ to leave an optical depth of $\tau_V \simeq 0.01$ or smaller that simply could not support such a luminous echo.

The only natural way to explain a sharp break in the optical light curve combined with a simultaneous rise of the near-IR emission to an almost identical luminosity is dust forming and becoming optically thick. It not only explains the simultaneity and the similar luminosities, but also the high dust temperatures because the temperature of newly forming dust is always close to the evaporation temperature of 1500–2000 K. Following Kochanek (2014) we can consider dust formation simply in terms of the 'blackbody' dust temperature $\sigma T_{bb}^4 = L/16\pi r^2$ set by the radiative flux. We will scale the results assuming dust forms at $T_{bb} = 1000 T_{bb3}$ K and discuss T_{bb} and the actual dust temperatures in more detail below. We will model the bolometric luminosity evolution as $L = 10^{43} L_{43} t_{300}^{-1/2}$ erg s^{-1} where $t = 300 t_{300}$ d is scaled to the approximate time of the break in the optical luminosity evolution.

As noted in other studies (e.g. Andrews et al. 2011; Gall et al. 2014; Fransson et al. 2014), dust cannot form in the material ejected during the transient because the dust temperature would be too high to form inside a radius

$$R \simeq 6 \times 10^{16} L_{43}^{1/2} T_{bb3}^{-2} t_{300}^{-1/4} \text{ cm} \quad (1)$$

that is much larger than the ejecta radius

$$R \simeq 5 \times 10^{15} v_{e2} t_{300} \text{cm} \quad (2)$$

until long after 300 d if it is expanding at $v_e = 2000 v_{e2}$ km s^{-1}. The evolution of these two radii is shown in Fig. 9, and the ejecta would not reach a large enough radius to allow dust formation until $t \simeq 2000$ d.

As discussed in Kochanek (2011), the re-obscuration of the transients SN 2008S and NGC 300 OT-2008 can be explained by dust re-condensing in their pre-existing dense winds. The CSM densities invoked to explain SN 2010jl are far denser than (even) the extreme AGB star winds invoked for these transients, although this is balanced by the far higher luminosities. Still, the optical and near-IR evolution of SN 2010jl strongly suggests that a similar process has occurred in SN 2010jl but under more extreme conditions. Inverting equation (1), the time at which dust can begin to form at a given radius is

$$t_{300}^{rad} = 0.12 L_{43}^2 R_{17}^{-4} T_{bb3}^{-8} \quad (3)$$

where $R = 10^{17} R_{17}$ cm. This is a very rapidly falling function of radius because the luminosity is dropping so slowly. In a wind with local density ρ_w where we can ignore the outward expansion on the growth time-scale t^{grow}, a grain can collisionally grow to radius $a = f v_c \rho_w t^{grow}/4\rho_b$ where $f = 0.01 f_2$ is the condensible mass fraction, $v_c = 1 v_{c1}$ km s^{-1} is the collision velocity and $\rho_b \simeq 2.2$ g cm^{-3} is the bulk density of the grains. If we define $\rho_w = \dot{M}/4\pi v_w R^2$ by a pre-existing wind characterized by a mass-loss rate $\dot{M} = \dot{M}_1$ M$_\odot$ yr^{-1} and wind velocity $v_w = 100 v_{w2}$ km s^{-1}, a grain grows to radius

$$a = 0.015 \frac{f_2 v_{c1} \dot{M}_1 t_{300}^{grow}}{v_{w2} R_{17}^{-2}} \ \mu\text{m}. \quad (4)$$

Very small grains have negligible visual opacities, so we can assume there is no significant absorption until $a > a_{min} = 0.001 a_{m3}$ μm. This then gives the required growth time at any given radius,

$$t_{300}^{grow} = 0.68 \frac{a_{m3} R_{17}^2 v_{w2}}{f_2 \dot{M}_1 v_{c1}}, \quad (5)$$

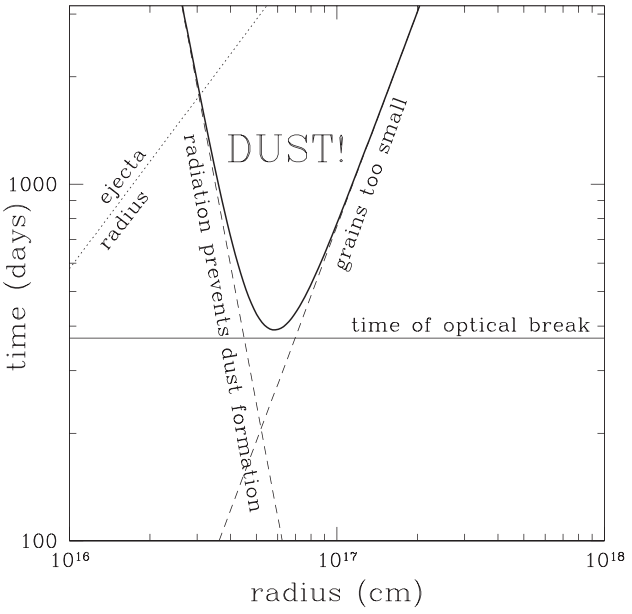

Figure 9. Scales related to dust formation. The steep, descending dashed line shows the time dependence of the radius at which the radiation will permit dust formation assuming $T_{bb3} = 1$ and setting $L_{43} = 0.64$ to match our estimate at $t_{300} = 1$ from Section 3.2. The ejecta radius (rising dotted line) does not enter the region where dust formation is possible until long after the observed time of the optical break at 370 d (horizontal solid line). For the mass-loss rate of $\dot{M}_1 = 0.27 v_{w2}$ invoked by Ofek et al. (2014), dust grains cannot have grown large enough to have a significant visual opacity below the second dashed line. At any given radius, dust will have a significant visual opacity only at times later than the sum of these two limits, which is given by the heavy solid curve. The resulting minimum time for dust formation is very close to the observed time-scale of the break in the optical light curve and the dramatic rise in the near-IR emission.

which is a rapidly rising function of radius. On small scales the radiation field keeps dust from forming and on large scales it simply grows too slowly. Fig. 9 shows these two time-scales, t_{300}^{rad} and t_{300}^{grow}, after setting $L_{43} = 0.64$ to match our estimate from Section 3.2 and $\dot{M}_1 = 0.27 v_{w2}$ to match the wind density from Ofek et al. (2014).

Thus, there is a significant dust opacity at any given radius only once $t > t^{form}(R) = t^{rad}(R) + t^{grow}(R)$, and Fig. 9 also shows the sum of these two time-scales. Because of the different radial scalings of t^{rad} and t^{grow}, there is a minimum time for dust formation. Moreover, without any particular manipulation of the parameters, this minimum time almost exactly matches the observed time of the optical break. If we minimize t_{form}, we find that the radius at which dust first reaches size a_{min} is

$$R_{17}^{min} \simeq 0.85 \frac{f_2^{1/6} L_{43}^{1/3} \dot{M}_1^{1/6} v_{c1}^{1/6}}{a_{m3}^{1/6} T_{bb3}^{4/3} v_{w2}^{1/6}} \quad (6)$$

and this occurs at time

$$t_{300}^{min} \simeq 0.73 \frac{a_{m3}^{2/3} L_{43}^{2/3} v_{w2}^{2/3}}{f_2^{2/3} \dot{M}_1^{2/3} T_{bb3}^{8/3} v_{c1}^{2/3}}. \quad (7)$$

If we identify this time-scale with the break in the light curve, $t_b = t^{min}$, then the required mass-loss rate of

$$\dot{M} \simeq 0.62 \frac{a_{m3} L_{43} v_{w2}}{f_2 v_{c1} T_{bb3}^4 t_{b300}^{3/2}} \text{ M}_\odot \text{ yr}^{-1} \quad (8)$$

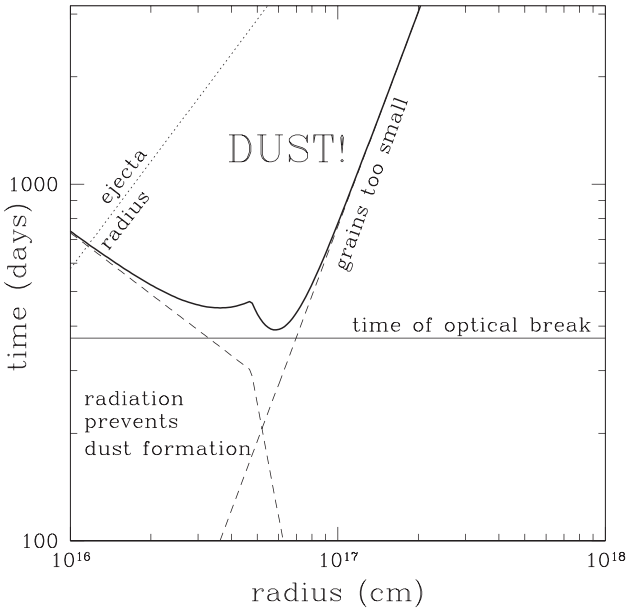

Figure 10. As in Fig. 9 but with the total luminosity breaking from $L \propto t^{-1/2}$ to $\propto t^{-7/2}$. Shortly after the luminosity break, dust formation will occur over a broad range of radii.

is quite close to the values of $\dot{M} \simeq 0.27 v_{\rm w2}$ and $\simeq 0.11 v_{\rm w2}$ $\rm M_\odot$ $\rm yr^{-1}$ invoked by Ofek et al. (2014) and Fransson et al. (2014) to explain the observed luminosity. Once there are grains of significant size $a > a_{\rm min}$, the optical depth becomes significant very quickly and there will always be hot, newly forming dust to support the near-IR emission.

We should note that if a dense CSM exists on these radial scales, the Ofek et al. (2014) and Fransson et al. (2014) scenarios for the origin of the break make dust formation near the time of the break even more inevitable. If either the total luminosity or the radiation temperature (or both) abruptly decrease, the radius outside of which dust formation is permitted drops precipitously compared to the scenario shown in Fig. 9. At these smaller radii the CSM densities are higher and the grain growth times are so short that dust formation occurs almost instantaneously once permitted by the radiation field. For example, Fig. 10 shows the effect of holding $T_{\rm bb}$ fixed but adding a break in the luminosity from roughly $L \propto t^{-1/2}$ to $L \propto t^{-7/2}$ as we found in Section 3.2. Shortly after the luminosity break, dust formation occurs over a broad range of radii by the time $t \simeq 1000$ d.

While our solution naturally explains the observations, its parameters are somewhat strained. First, given the high radiation temperature (8000–9000 K) a dust formation temperature of $T_{\rm bb} \simeq 500$ K seems more likely than the $T_{\rm bb} = 1000$ K we have used in the scaling solutions (see Kochanek 2014). But lowering $T_{\rm bb}$ by a factor of 2 would require raising $\dot{M}$ by a factor of 16 to keep the $t^{\rm min}$ fixed. Note that the dust emission would still be very hot even at $T_{\rm bb} \simeq 500$ K because the smallest forming grains would be stochastically heated to temperatures close to their evaporation temperatures and would radiate most of their energy in these temperature spikes (see Kochanek 2014). Secondly, once dust forms, the optical depth becomes very high, with

$$\tau_{\rm V} \simeq 600 \frac{\kappa_{\rm V2} \dot{M}_1^{5/6} a_{m3}^{1/6} T_{\rm bb3}^{4/3}}{f_2^{1/6} v_{\rm c1}^{1/6} v_{\rm w2}^{5/6} L_{43}^{1/3}} \quad (9)$$

where we have scaled the visual opacity to $\kappa_{\rm V} = 100 \kappa_{\rm V2}$ $\rm cm^2$ $\rm g^{-1}$ and this would be the optical depth for a wind extending from $R^{\rm min}$ outwards. If it forms in a finite annulus, the optical depth is reduced by $1 - R_{\rm in}/R_{\rm out}$ which will quickly become a modest correction (see Fig. 9). Empirically, the observed optical depths are far smaller.

A plausible solution is that the CSM has significant density inhomogeneities. For example, if we drop the required $T_{\rm bb}$ to 500 K and keep $\dot{M}$ fixed while putting fraction $F = 0.01$ of the CSM in clumps with an over-density of $\xi = 16$, then dust will only form in the dense clumps and the mean optical depth would drop by the factor F. The effective drop would be still larger because of photons escaping by scattering though the low-density regions. Combined with the possibilities allowed by the global asymmetries invoked by other studies of this system, this provides a means of making the properties of our solution less extreme.

5 SUMMARY AND CONCLUSIONS

The luminous and long-lived Type IIn SN 2010jl shows strong evidence for the interaction of the SN ejecta with a dense, hydrogen-rich CSM shell. We obtained 12 optical spectra between $t = 55$ and 909 d, which adds significant coverage to the spectroscopic time sequence for this event. We also obtained an epoch of late time *BVRI* photometry, and derived a semi-bolometric, optical light curve through $t = 775$ d.

Analysis of the spectra revealed NW (FWHM $\sim$ 100 $\rm km\,s^{-1}$) emission features of H and He associated with the slowing expanding CSM shell, ionized by the initial flash of the SN. The IW (FWHM $\sim$1000–2000 $\rm km\,s^{-1}$) component of the Balmer lines also showed complex evolution, particularly a progressive blueshift for at least the first $\sim$150 d, and a pronounced asymmetry after $\sim$750 d. These observations are not fully consistent with any emission and broadening mechanisms yet proposed, including continued post-shock dust formation and electron scattering in an optically thick medium.

The optical light curve exhibits a steep drop off for $t \gtrsim 300$ d that has been interpreted as a transition of the SN to the snow-plow phase, or as the emergence of the shock from the CSM. However, in light of the timing coincidence of the break in the optical and rise in the NIR light curves, the most natural interpretation is that the optical light from continued CSM interactions begins to be reprocessed into the NIR after the break. Using a simple collisional model for dust growth, we find that dust naturally reforms in the dense, pre-existing CSM wind on the observed time-scale of the breaks in the optical and near-IR light curves without any finetuning of the parameters. The model would be improved if the CSM is significantly clumpy, consistent with suggestions that it has more complex structure (e.g. Chandra et al. 2012a; Maeda et al. 2013; Fransson et al. 2014; Ofek et al. 2014). We also emphasize that this interpretation indicates continued strong interactions of the SN ejecta and the CSM for $\gtrsim$2.5 yr.

Finally, we note that a number of observational changes in the evolution of SN 2010jl are approximately coincident with the optical break and rise in the NIR light, including the decline in the Hα luminosity, the loss of a broad, high-velocity component in the Balmer emission profiles and subsequent narrowing of the lines, and the recession in the blueshift of Hα. Despite the wealth of studies in the literature dedicated to this fascinating object, the details of the true nature of SN 2010jl's evolution remain controversial, emphasizing the importance of multiwavelength and continuous monitoring of such events.

ACKNOWLEDGEMENTS

We thank the referee, Nathan Smith, for his helpful comments and suggestions. We would also like to thank Matthew Penny and Dale Mudd for their helpful discussion and assistance in data acquisition and analysis.

This material is based upon work supported by the National Science Foundation Graduate Research Fellowship under Grant No. DGE-1144469. BS is supported by NASA through the Hubble Fellowship grant HST-HF-51348.001 awarded by the Space Telescope Science Institute, which is operated by the Association of Universities for Research in Astronomy, Inc., for NASA, under contract NAS 5-26555. Support for JLP is in part by FONDECYT through the grant 1151445 and by the Ministry of Economy, Development, and Tourisms Millennium Science Initiative through grant IC120009, awarded to The Millennium Institute of Astrophysics, MAS.

This work is based on observations obtained at the MDM Observatory, operated by Dartmouth College, Columbia University, Ohio State University, Ohio University, and the University of Michigan. OSMOS has been generously funded by the National Science Foundation (AST-0705170) and the Center for Cosmology and AstroParticle Physics at The Ohio State University. Based on observations obtained with the APO 3.5-metre telescope, which is owned and operated by the Astrophysical Research Consortium. The LBT is an international collaboration among institutions in the United States, Italy and Germany. LBT Corporation partners are: The Ohio State University, and The Research Corporation, on behalf of The University of Notre Dame, University of Minnesota and University of Virginia; The University of Arizona on behalf of the Arizona university system; Istituto Nazionale di Astrofisica, Italy; LBT Beteiligungsgesellschaft, Germany, representing the Max-Planck Society, the Astrophysical Institute Potsdam, and Heidelberg University. This paper used data obtained with the MODS spectrographs built with funding from NSF grant AST-9987045 and the NSF Telescope System Instrumentation Program (TSIP), with additional funds from the Ohio Board of Regents and the Ohio State University Office of Research.

Funding for the SDSS and SDSS-II has been provided by the Alfred P. Sloan Foundation, the Participating Institutions, the National Science Foundation, the U.S. Department of Energy, the National Aeronautics and Space Administration, the Japanese Monbukagakusho, the Max Planck Society, and the Higher Education Funding Council for England. The SDSS Web Site is http://www.sdss.org/. The SDSS is managed by the Astrophysical Research Consortium for the Participating Institutions. The Participating Institutions are the American Museum of Natural History, Astrophysical Institute Potsdam, University of Basel, University of Cambridge, Case Western Reserve University, University of Chicago, Drexel University, Fermilab, the Institute for Advanced Study, the Japan Participation Group, Johns Hopkins University, the Joint Institute for Nuclear Astrophysics, the Kavli Institute for Particle Astrophysics and Cosmology, the Korean Scientist Group, the Chinese Academy of Sciences (LAMOST), Los Alamos National Laboratory, the Max-Planck-Institute for Astronomy (MPIA), the Max-Planck-Institute for Astrophysics (MPA), New Mexico State University, Ohio State University, University of Pittsburgh, University of Portsmouth, Princeton University, the United States Naval Observatory, and the University of Washington.

This research has made use of the NASA/IPAC Extragalactic Database, which is operated by the Jet Propulsion Laboratory, California Institute of Technology, under contract with the National Aeronautics and Space Administration.

REFERENCES

Abazajian K. N. et al., 2009, MNRAS, 351, 1071
Andrews J. E. et al., 2011, AJ, 142, 45
Benetti S., Bufano F., Vinko J., Marion G. H., Pritchard T., Wheeler J. C., Chatzopoulos E., Shetrone M., 2010, Central Bureau Electron. Telegrams, 2536, 1
Bessell M. S., Castelli F., Plez B., 1998, A&A, 333, 231
Blanton M. R., Roweis S., 2007, AJ, 133, 734
Borish H. J., Huang C., Chevalier R. A., Breslauer B. M., Kingery A. M., Privon G. C., 2015, ApJ, 801, 7
Burrows D. N. et al., 2005, Space Sci. Rev., 120, 165
Chandra P., Chevalier R. A., Irwin C. M., Chugai N., Fransson C., Soderberg A. M., 2012a, ApJ, 750, L2
Chandra P., Chevalier R. A., Chugai N., Fransson C., Irwin C. M., Soderberg A. M., Chakraborti S., Immler S., 2012b, ApJ, 755, 110
Chevalier R. A., Fransson C., 1994, ApJ, 420, 268
Chugai N. N., 2001, MNRAS, 326, 1448
Chugai N. N., Danziger I. J., 1994, MNRAS, 268, 173
Chugai N. N., Blinnikov S. I., Fassia A., Lundqvist P., Meikle W. P. S., Sorokina E. I., 2002, MNRAS, 330, 473
Chugai N. N. et al., 2004, MNRAS, 352, 1213
Cohen M., Wheaton W. A., Megeath S. T., 2003, AJ, 126, 1090
Dessart L., Hillier D., Gezari S., Basa S., Matheson T., 2009, MNRAS, 394, 21
Filippenko A., 1997, ARA&A, 35, 309
Fox O. D., Filippenko A. V., Skrutskie M. F., Silverman J. M., Ganeshalingam M., Cenko S. B., Clubb K. I., 2013, ApJ, 146, 2
Fransson C. et al., 2014, ApJ, 797, 118
Gal-Yam A., 2012, Science, 337, 927
Gall C. et al., 2014, Nature, 511, 326
Immler S., Milne P., Pooley D., 2010, Astron. Telegram, 3012, 1
Ivezić Ž. et al., 2007, in Sterken C., ed., ASP Conf. Ser. Vol. 364, The Future of Photometric, Spectrophotometric and Polarimetric Standardization. Astron. Soc. Pac., San Francisco, p. 165
Kochanek C. S., 2011, ApJ, 741, 37
Kochanek C. S., 2014, preprint (arxiv:1407.7856)
Kozłowski S. et al., 2010, ApJ, 722, 1624
Laor A., Draine B. T., 1993, ApJ, 402, 441
Li W. et al., 2011, MNRAS, 412, 1441
Maeda K. et al., 2013, ApJ, 776, 5
Martini P. et al., 2011, PASP, 123, 187
Neill J. D. et al., 2011, ApJ, 727, 15
Newton J., Puckett T., 2010, Central Bureau Electron. Telegrams, 2532, 1
Ofek E. O. et al., 2014, ApJ, 781, 42
Patat F., Taubenberger S., Benetti S., Pastorello A., Harutyunyan A., 2011, A&A, 527, L6
Pigulski A., Pojmański G., Pilecki B., Szczygieł D. M., 2009, Acta Astron., 59, 33
Pogge R. W. et al., 2010, in McLean I. S., Ramsay S. K., Takami H., eds, Proc. SPIE, Vol. 7735, Ground-Based and Airborne Instrumentation for Astronomy III. SPIE, Bellingham, p. 77350A
Pojmański G., 2002, Acta Astron., 52, 397
Salamanca I., Cid-Fernandes R., Tenorio-Tagle G., Telles E., Terlevich R. J., Muñoz-Tuñón C., 1998, MNRAS, 300, L17
Salamanca I., Terlevich R. J., Tenorio-Tagle G., 2002, MNRAS, 330, 844
Schlafly E. F., Finkbeiner D. P., 2011, ApJ, 737, 103
Schlegel E. M., 1990, MNRAS, 244, 269
Smartt S. J., Eldridge J. J., Crockett R. M., Maund J. R., 2009, MNRAS, 395, 1409
Smith N., Chornock R., Silverman J. M., Filippenko A. V., Foley R. J., 2010, ApJ, 709, 856
Smith N., Li W., Filippenko A. V., Chornock R., 2011a, MNRAS, 412, 1522
Smith N. et al., 2011b, ApJ, 732, 63
Smith N., Silverman J. M., Filippenko A. V., Cooper M. C., Matheson T., Bian F., Weiner B. J., Comerford J. M., 2012, AJ, 143, 17
Stetson P. B., 1987, PASP, 99, 191

Stoll R. et al., 2010, in McLean I. S., Ramsay S. K., Takami H., eds, Proc. SPIE, Vol. 7735, Ground-Based and Airborne Instrumentation for Astronomy III. SPIE, Bellingham, 77354L-PLX5
Stoll R., Prieto J. L., Stanek K. Z., Pogge R. W., Szczygieł D. M., Pojmanski G., Antognini J., Yan H., 2011, ApJ, 730, 34
Svirski G., Nakar E., Sari R., 2012, ApJ, 759, 108
van Dokkum P. G., 2001, PASP, 113, 1420
Yamanaka M., Okushima T., Arai A., Sasada M., Sato H., 2010, Central Bureau Electron. Telegrams, 2539, 1
Yaron O., Gal-Yam A., 2012, PASP, 124, 668
Zhang T. et al., 2012, AJ, 144, 131

SUPPORTING INFORMATION

Additional Supporting Information may be found in the online version of this article:

Table 3. Optical luminosity.
(http://www.mnras.oxfordjournals.org/lookup/suppl/doi:10.1093/mnras/stv2795/-/DC1).

Please note: Oxford University Press is not responsible for the content or functionality of any supporting materials supplied by the authors. Any queries (other than missing material) should be directed to the corresponding author for the article.

This paper has been typeset from a TEX/LATEX file prepared by the author.